micromachines

MDPI

Article

RETRACTED: Design and Dynamic Simulation of a Novel Traveling Wave Linear Ultrasonic Motor

Lin Yang [1], Kaixi Yao [1], Weihao Ren [1,*], Liang Chen [2], Mojian Yang [3], Rongcheng Zhao [3] and Siyu Tang [3]

[1] State Key Laboratory of Mechanics and Control of Mechanical Structures, Nanjing University of Aeronautics and Astronautics, Nanjing 211106, China; yanglin@nuaa.edu.cn (L.Y.); cathyyao@nuaa.edu.cn (K.Y.)
[2] Innovation Academy for Microsatellites of Chinese Academy of Sciences, Shanghai 201210, China; chen15951991306@163.com
[3] Nuaa Super Control Technology Co., Ltd., Nanjing 211100, China; yangmojian@126.com (M.Y.); rch_zhao@126.com (R.Z.); tangsiyu1217@126.com (S.T.)
* Correspondence: renweihao@nuaa.edu.cn

Abstract: To overcome the problem of frequency consistency and simplify the design process of linear ultrasonic motor, a novel traveling wave linear ultrasonic motor with a ring-type stator is proposed in this paper. The combination of two orthogonal bending vibration modes with the same order is selected as the operating mode of the motor. A traveling wave along the side of the stator is utilized to drive the slider to move linearly. The stator adopts a ring symmetrical structure, which can effectively ensure that the resonance frequencies of the two vibration modes are consistent. Thus, we do not need to tune the frequencies of the two vibrations by constantly adjusting the shape of the stator or designing complex clamping parts to fix the stator without making any influence on the vibrations. Meanwhile, a three-dimensional finite element model of the motor is built. Using the model, we obtain the elliptical motion trajectories of the stator driving surface, the output performance of the motor, the sticking-slipping-separation contact characteristic between the stator and the slider and fabricate and measure a prototype of the proposed motor.

Keywords: linear ultrasonic motors; traveling wave; finite element model; dynamic simulation; contact characteristic

check for updates

Citation: Yang, L.; Yao, K.; Ren, W.; Chen, L.; Yang, M.; Zhao, R.; Tang, S. RETRACTED: Design and Dynamic Simulation of a Novel Traveling Wave Linear Ultrasonic Motor. *Micromachines* **2022**, *13*, 557. https://doi.org/10.3390/mi13040557

Academic Editor: Dalius Mažeika

Received: 27 March 2022
Accepted: 29 March 2022
Published: 31 March 2022
Retracted: 11 September 2025

Publisher's Note: MDPI stays neutral with regard to jurisdictional claims in published maps and institutional affiliations.

Copyright: © 2022 by the authors. Licensee MDPI, Basel, Switzerland. This article is an open access article distributed under the terms and conditions of the Creative Commons Attribution (CC BY) license (https://creativecommons.org/licenses/by/4.0/).

1. Introduction

With the discovery of piezoelectric ceramics in the 1940s, ultrasonic motors (USMs) based on the converse piezoelectric effect of piezoelectric ceramics came into being [1]. As a new type of motor, USMs have many distinctive merits such as compact structure, self-locking, quick response, higher position accuracy, etc., which makes them have widespread prospects in some precision positioning systems, including aerospace, optical instrument, micro-robot, medical instruments, and so on [2–7]. The linear ultrasonic motor (LUSM), as an important branch of USMs, has also developed rapidly in recent years.

Up to now, a great deal of LUSMs have been proposed with different working principles and variable shapes [8–14]. According to the way the elliptical motion trajectory is formed on the drive foot, the linear ultrasonic motors can be divided into single-mode motors and composite mode motors. For composite mode linear ultrasonic motors, the two vibration modes need to be excited concurrently with the same frequency in the stator to superpose and generate an elliptical motion at the driving surface. However, since the stator of this composite motor structure is generally an asymmetric rod or plate, it takes a lot of time to design and optimize the stator to excite two modes with the same frequency. Even so, the stator design is affected by the machining and assembly, and the actual frequency difference between the two modes may be different from the theoretical calculation. In order to avoid the complex process of designing the stator in composite mode LUSM, researchers proposed single-mode LUSMs that utilize a single vibration mode

RETRACTED

This paper has been retracted. A retraction notice was published on 11 September 2025 in *Micromachines* **2025**, *16*, 1041. https://doi.org/10.3390/mi16091041

as the operating mode to drive the slider in various directions of motion [15–17]. However, for this kind of motor, it needs to reduce the influence on the stator's vibration, which means the clamping part should be well-designed. Usually, it should be designed as a flexible structure and be placed coincident with the node plane of vibration modes, which may bring certain restrictions to the structural design of the LUSMs.

It is well known that traveling wave rotary ultrasonic motors (TRUMs) [18–20] are probably the most successful motors, and they have been commercialized in many fields with stable performance, such as Canon cameras. The ring-type stator of this motor is a symmetrical structure that can easily achieve the frequency consistency of two bending vibration modes with the same order. Moreover, the out-of-plane modes of this type of stator include node circles and node diameters [1], and the node circle can be utilized to fix the stator without designing redundant clamping parts, which makes the stator fixed quite flexible.

In the light of the advantages of this ring-type stator, a novel traveling wave LUSM with a symmetrical structure is proposed in this paper. The novel traveling wave LUSM utilizes the superposition of two orthogonal bending vibration modes with the same order to generate a traveling wave at the stator, which drives the slider into linear motion through preload. Since the symmetry of this stator's structure can be easily guaranteed, the frequency consistency of two bending vibration modes is relatively easy to achieve. And the method of fixing the stator is similar to the TRUMs, which simplifies the design process and does not need to design any redundant clamping part.

To verify the novel traveling wave LUSM's operating principle and study its dynamic characteristics, a three-dimensional finite element model is built by the finite element method (FEM). Firstly, the stator's bending vibration modes are acquired by modal analysis, and the elliptic motion trajectory of the stator's driving surface is obtained by transient dynamic analysis. Secondly, the output performance and the start-stop transient characteristics of the motor are simulated by this model. Meanwhile, the prototype is fabricated, and the vibration characteristics of the stator and output performance of the motor are also measured through experiments. Thirdly, the actual contact characteristics between the stator and the slider are discussed from different perspectives in detail to comprehend the driving mechanism of the motor.

2. Structure and Operating Principle of the Motor

2.1. The Structure of Traveling Wave LUSM

An explosion view of the stator is shown in Figure 1a. The stator whose greatest external diameter is 33 mm and the height is 14 mm is mainly composed of a hollow cylinder and two ring-type plates. Thirty teeth are uniformly processed along the side of the cylinder through the milling machine. Two ring-type plates are bonded on both ends of the cylinder symmetrically. It is worth noting that three threaded holes are set on the inner rings of each ring-type plate for fixing the stator. A prototype of the stator has been fabricated and assembled, as shown in Figure 1b.

Figure 2a illustrates the three-dimensional structure model of the proposed traveling wave LUSM. It mainly comprises the stator, a slice of friction material, two PZT rings, a slider, a motion platform, four guideways, a preload bolt, a flexible fixing part, etc. The overall structure is like a cube with a length of 59 mm, a width of 52 mm, and a height of 51.5 mm. The friction material is bonded on the stator tooth surface instead of the slider. Meanwhile, its internal structure is seen in the section view of Figure 2b. Two PZT rings with an inner diameter and outer diameter of 20 mm and 30 mm respectively, and thickness of 0.5 mm are bonded on both ends of the stator symmetrically while a slider is bolted to the motion platform. The motion platform is fixed on the base through the guideways to ensure its linear motion. The stator is fixed on a flexible fixing part by several screws. In addition, the base with four slide slots provides one degree of freedom perpendicular to the direction of the platform's movement for the fixing part. In other words, the stator can

RETRACTED

only move in one direction. Moreover, the proposed traveling wave LUSM applies a bolt to adjust the preload between the slider and the driving surface.

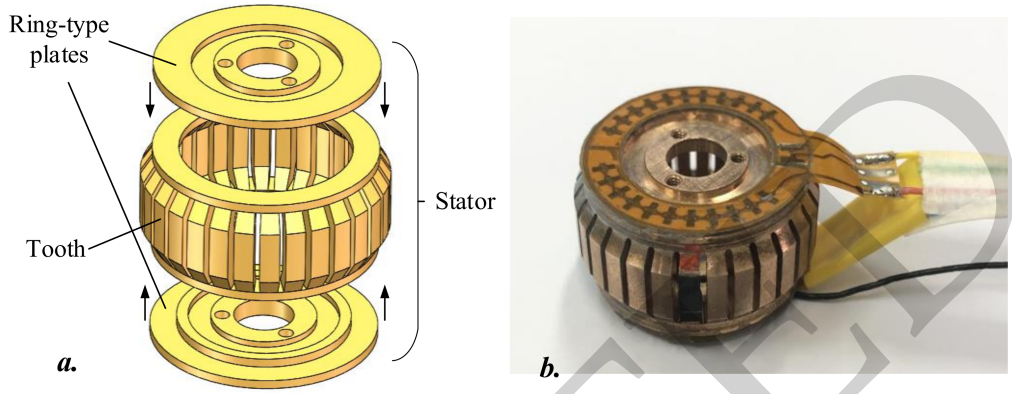


Figure 1. Proposed stator: (**a**) explosion view; (**b**) prototype.

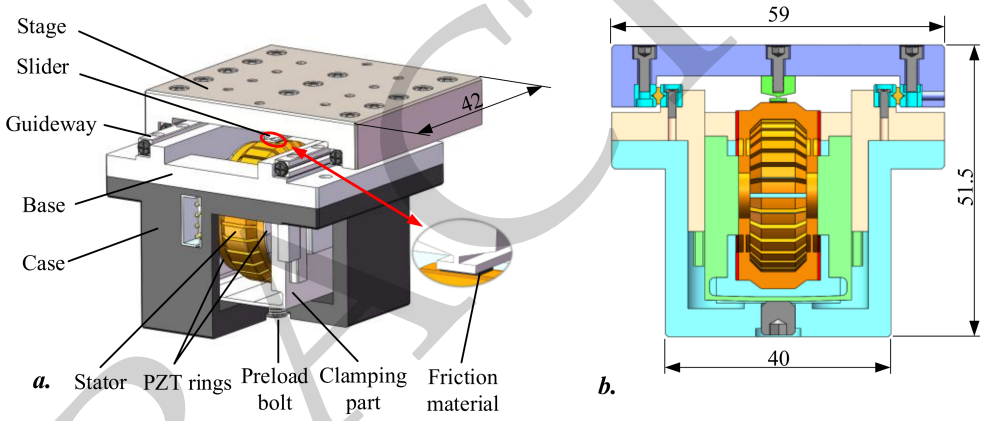


Figure 2. Structure of the proposed traveling wave LUSM: (**a**) three-dimensional model; (**b**) section view.

2.2. The Operating Principle of Traveling Wave LUSM

For a cylindrical stator, any in-plane mode of any order can be used as the working mode of the motor in theory, but we prefer a mode of the lower order as the working mode. On the one hand, higher-order needs a higher frequency of the excitation signal. Besides, there will be a lot of interference modes near the working mode of high frequency, which makes it difficult to perform modal analysis, thus making the superimposed obtained traveling wave impure and unfavorable to the operation of the motor. On the other hand, the higher mode consumes more energy through damping.

In this novel design, B_{05} bending vibration modes were selected as operating modes of the motor, as shown in Figure 3. Two orthogonal in-plane B_{05} modes formed on the side of the stator are displayed in Figure 3a while two orthogonal out-of-plane B_{05} modes formed on both ends of the stator are demonstrated in Figure 3b,c respectively. In other words, an in-plane B_{05} mode and an out-of-plane B_{05} mode exist simultaneously on the stator. Here, we call them Mode-A, while the other orthogonal mode is called Mode-B.

To excite Mode-A and Mode-B, two PZT rings that are divided into a series of sector areas and polarized are bonded on both ends of the stator symmetrically, which are divided into four groups A, B, C, and D; see in Figure 4. Positive (+) and negative (−) signs show the polarization directions of sector areas that are along the positive direction of the *Z*-axis. The four phases of alternating voltages with equal amplitude, equal frequency, and phase differences of 0, $\pi/2$, π, and $3\pi/2$ are applied to groups A, B, C, and D, respectively. When frequencies of alternating voltages are set to coincide with the resonance frequency of the stator, Mode-A can be excited by Group A and D, and Mode-B can be excited by Group B

RETRACTED

and C. Thus, a traveling wave can be formed by the superposition of Mode-A and Mode-B. Another key thing to remember is that the traveling wave along the side of the stator is utilized to generate the elliptical motion at driving feet, which can drive the slider into linear motion through preload.

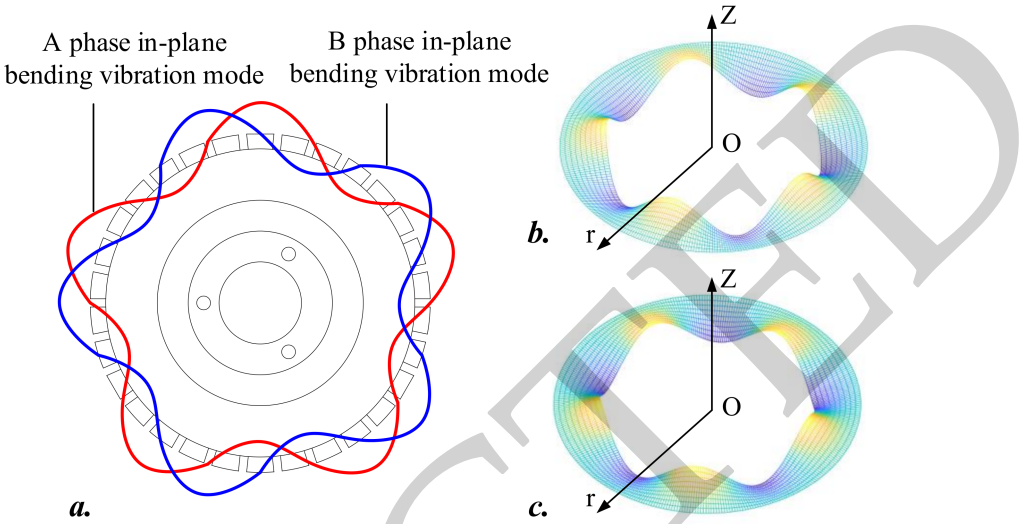


Figure 3. Operating modes of the motor: (**a**) in-plane B_{05} bending vibration modes; (**b**) A phase out-of-plane B_{05} bending vibration mode; (**c**) B phase out-of-plane B_{05} bending vibration mode.

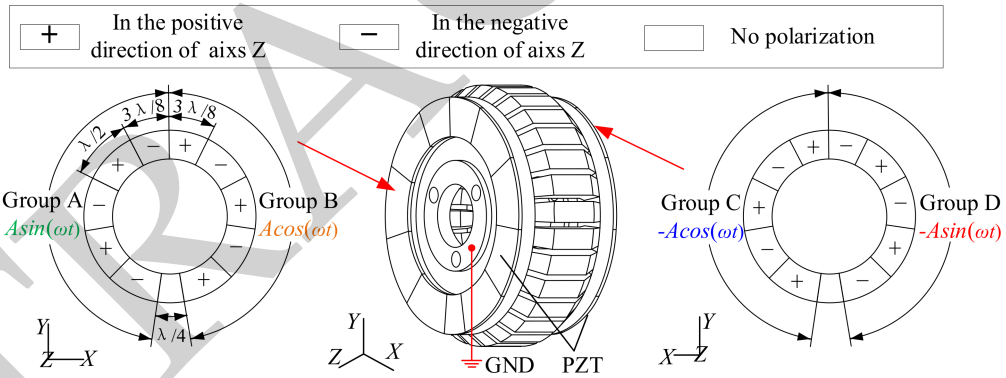


Figure 4. Polarization pattern and distribution of PZT rings.

To demonstrate the operating mechanism, one cycle of the driving process of the motor is presented in Figure 5, where four limit positions of point P on the driving tooth are extracted. After applying the alternating voltages, the traveling wave along the side of the stator propagates in the counterclockwise direction. Similarly, the motion trajectory of point P is also a counterclockwise ellipse. One cycle later, the traveling wave moves a wavelength and point P returns to its initial position, whereas the slider moves a certain distance to the right. It should be noted that the motion trajectory of each tooth on the stator is an ellipse; thus, anyone can be selected as the driving tooth.

The above process is the case of the slider to the left, if the above electrical signals applied to Group A, B, C, and D are changed to Acos(ωt), Asin(ωt), -Asin(ωt), -Acos(ωt), at this time Mode-B can be excited by Group A and D, and Mode-A can be excited by Group B and C. Thus, the phase reversed, and the traveling wave on the stator will propagate in the clockwise direction, then the slider moves to the right motion.

RETRACTED

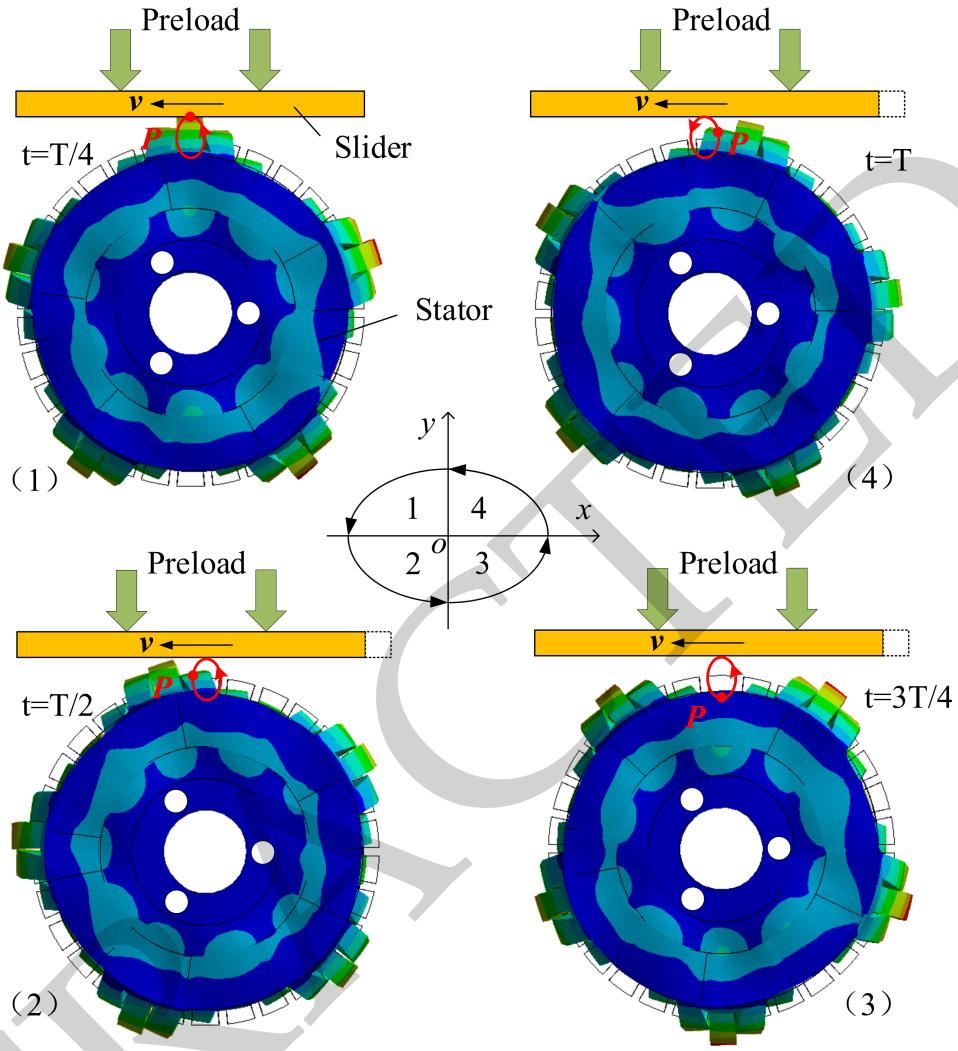


Figure 5. Operating mechanism of the motor.

3. Dynamic Simulation and Experimental Confirmation of the Motor

To study the motor's dynamic characteristics and contact characteristics, ADINA is used to establish the overall dynamic model of the experimental prototype. By the model, the output characteristic (velocity, load, etc.) and contact characteristic of the motor can be obtained, which is significate for its initial design and performance optimization in the future study.

A simplified three-dimensional finite element model of the proposed LUSM is demonstrated in Figure 6, which is mainly composed of a stator (33,990 hexahedron elements), a slice of friction material (48 hexahedron elements), two PZT rings (1200 hexahedron elements), a slider (1080 hexahedron elements), a guideway (1440 hexahedron elements) and a fixing part (14,070 hexahedron elements). The material parameters employed in the model are phosphor bronze for the stator, aluminum for the slider, guideway and fixing part, PTFE for the friction material, and PZT-8 presented by the built-in material model in ADINA for the PZT. The relevant material parameters are listed in Tables 1 and 2 [21,22]. The Coulomb friction coefficient between the friction material and the slider utilized in the following simulation is 0.3, and the Coulomb friction coefficient between slider and guideway is 0.001. Meanwhile, the damping ratio utilized in the simulation model is 0.0008, which is obtained by the empirical value [18].

RETRACTED

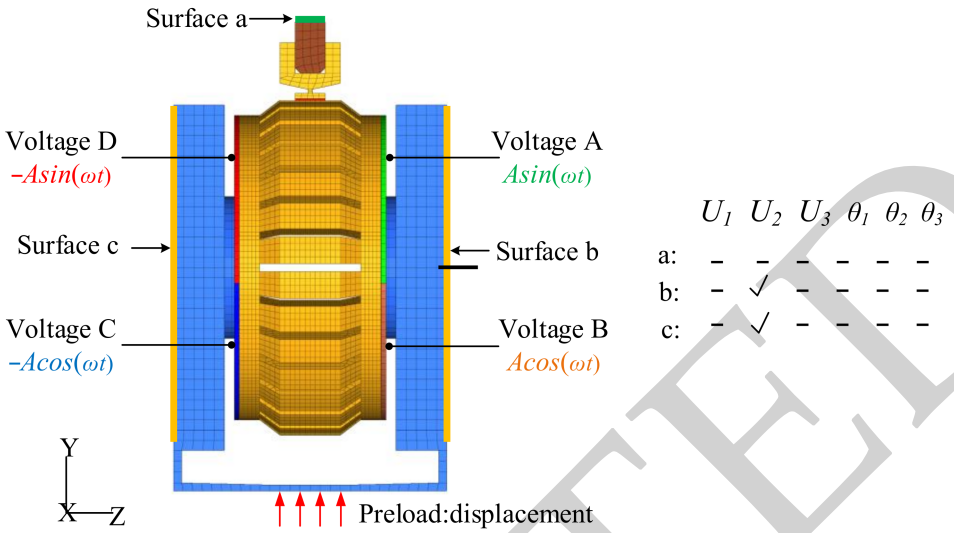


Figure 6. 3D finite element model of the traveling wave LUSM.

Table 1. Constants of the common materials.

Material	Phosphor Bronze	Aluminum	PTFE
Density (kg/m^3)	8780	2780	2100
Poisson's ratio	0.33	0.33	0.3
Young's modulus (N/m^2)	1.15×10^{11}	7.1×10^{10}	1.2×10^{9}

Table 2. Electro-mechanical properties of the piezoelectric material.

Piezoelectric Model		
Density (kg/m^3)		7500
Poisson's ratio	v_{12}	0.35
	$v_{13} = v_{23}$	0.38
Young's modulus (N/m^2)	$E_1 = E_2$	6.1×10^{10}
	E_3	5.32×10^{10}
Shear modulus (N/m^2)	G_{12}	2.26×10^{10}
	$G_{13} = G_{23}$	2.11×10^{10}
Piezoelectric coupling constants (C/m)	$e_{13} = e_{23}$	−7.209
	e_{33}	15.118
	$e_{51} = e_{62}$	12.332
Dielectric constants (C/(Vm))	$\varepsilon_{11} = \varepsilon_{22}$	1.53×10^{-8}
	ε_{33}	1.5×10^{-8}

The three-dimensional finite element model's boundary conditions and loadings are set up according to the actual condition as shown in Figure 6. Based on not affecting the calculation accuracy the stator and the fixing part are glued together, which can reduce the number of contact pairs. Similarly, to reduce the computational cost, we ignore the contact of the fixing part with the base. For instance, in actual operation, the guide rail is fixed to the base and the movable sub slides on the rail; meanwhile, when the motor is working, the whole part composed of the stator and the fixed part will have vibration displacement in the Y direction. So, in the simulation, the fixing part only has degrees of freedom in the Y direction, and all the degrees of freedom of the guideway are constrained. To simulate the preload, a certain displacement is given to the bottom plane of the fixing part. And four phases of alternating voltages are applied to the corresponding regions of the PZT rings.

RETRACTED

3.1. Modal Analysis

The resonance frequencies and bending vibration shapes of Mode-A and Mode-B have shown in Figure 7 stem from the modal analysis of the stator by ADINA. It demonstrates two orthogonal in-plane B_{05} bending vibration shapes, whose resonance frequencies are 52,241 Hz and 52,247 Hz, respectively. The simulation results show that the difference between the two resonant frequencies is 6 Hz, indicating that the stator has a fine frequency consistency.

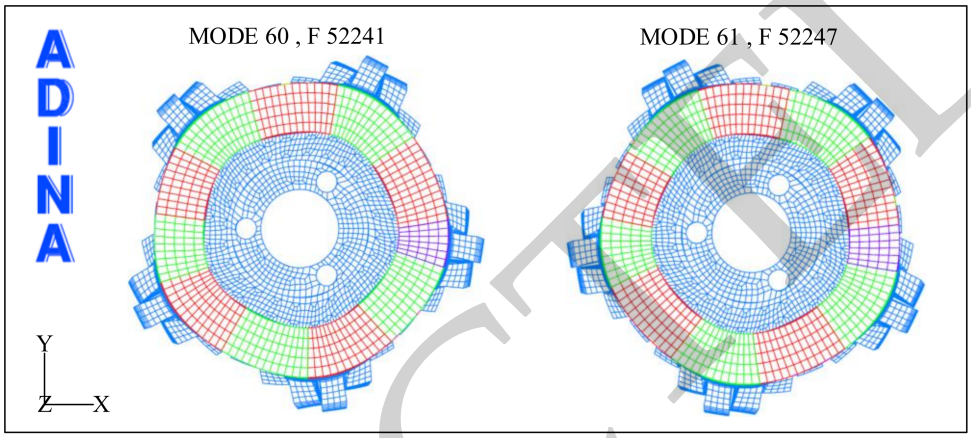


Figure 7. Operating modes of the stator in the simulation.

Furthermore, the bending vibration shapes and the resonance frequencies of the stator measured by Laser Doppler Vibrometer (PSV-300F-B; Polytec Ltd., Baden-Württemberg, Germany) under a $100V_{P\text{-}P}$ voltage are shown in Figures 8 and 9. To clearly describe the bending vibration shapes of Mode-A, two regions are selected for vibration measurement: the first one is one tooth surface on the stator, whereas the other one is the end surface of the stator on which the PZT rings are bonded. The bending vibration shapes of Mode-A presented in Figure 8 indicate an in-plane up-down bending movement measured on the tooth surface, while the end surface of the stator exists an out-of-plane standing wave with five wave peaks. One point should be noted that the two bending vibration shapes are generated together. Hence, the bending vibration modes on the stator include out-of-plane and in-plane 5th order bending vibration mode, which is coincident with the operating principle of the proposed traveling wave LUSM. Since the vibration shape of Mode-B is the same as Mode-A, no detailed analysis will be made here. The resonance frequencies of Mode-A and mode B are tested to be 52,062 Hz and 52,093 Hz, respectively, which is close to that of the simulation. From the results, frequency consistency of the stator's structure is easily achieved. In theory, the magnitude of vibration velocities of mode A and mode B should be the same, but in the measurement, they are not the same, the reason may be related to the different angles of the reference point during the test.

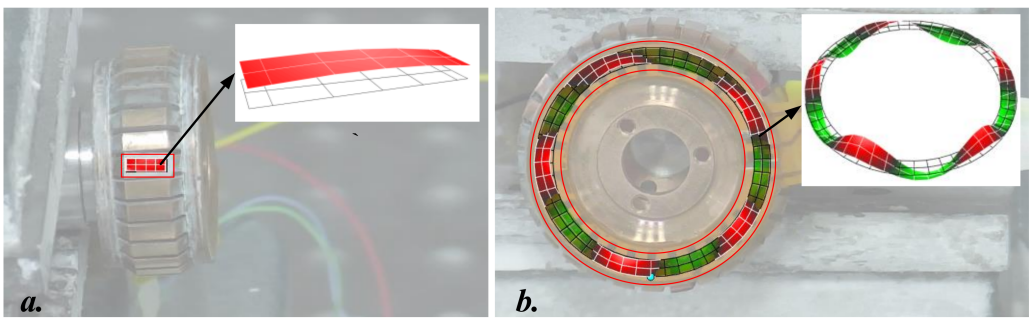


Figure 8. Vibration scanning results of the stator: (**a**) vibration shape of one tooth surface; (**b**) vibration shape of the stator end surface.

RETRACTED

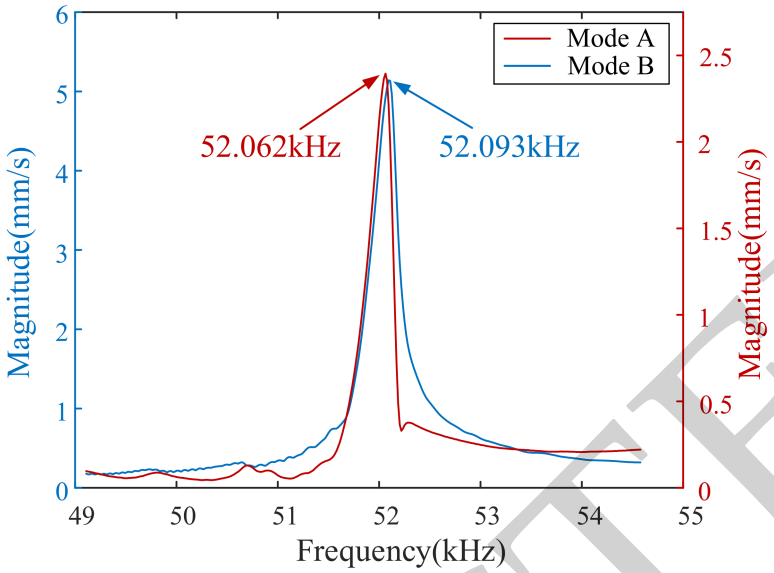


Figure 9. Measured vibration velocity response spectrum.

3.2. Transient Dynamic Analysis

To test the vibration characteristics of the motor, three points distributed on the center of the driving surface along the *X*-axis are selected, as shown in Figure 10a. Under the condition that the peak-to-peak value of the voltage is 500 V, the frequency is 52.2 kHz and the damping ratio is 0.008, the elliptical motion trajectories of three points on the driving surface under a steady state are shown in Figure 10b–d. On the XY-plane, the amplitude of point 1 in the *X*-axis (tangential direction) is 3.5 μm, and that in the *Y*-axis (normal direction) is 6.2 μm. Meanwhile, the amplitudes of point 1, point 2, and point 3 decrease sequentially. However, the maximum amplitude of these three points in the *Z*-axis is only about 0.025 μm and it makes no effect on driving the slider in the *Z*-axis direction.

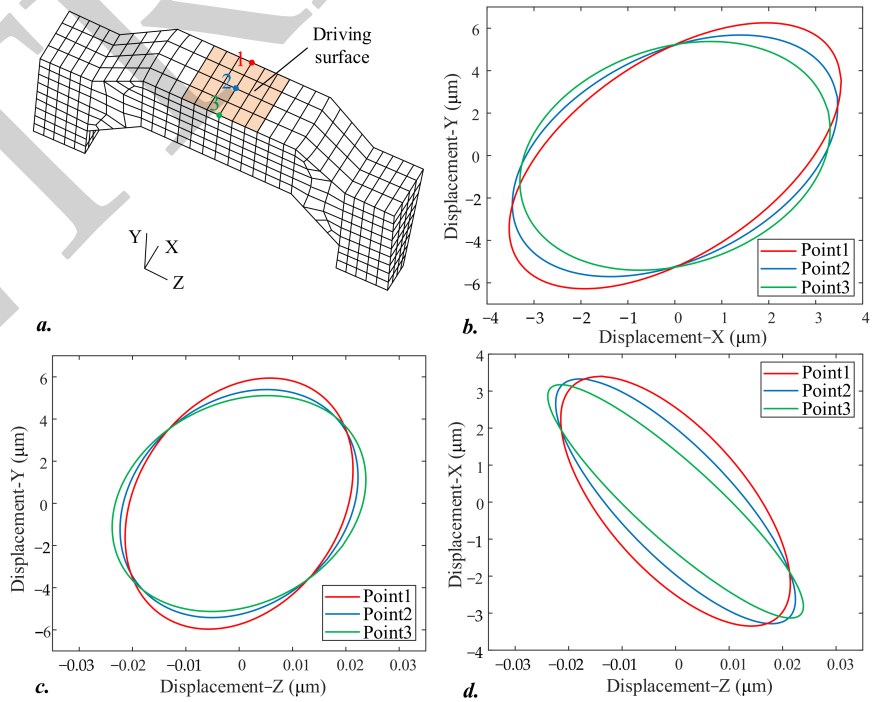


Figure 10. Elliptical motion trajectories of three points on the driving surface: (**a**) 3D mesh model of one stator tooth; (**b**) elliptical motion trajectory on XY-plane; (**c**) elliptical motion trajectory on ZY-plane; (**d**) elliptical motion trajectory on ZX-plane.

RETRACTED

To verify the working principle of the proposed motor and evaluate its output performance, we have selected four groups of different preloads of 30 N, 40 N, 50 N, and 60 N (500Vp-p, 52.2 kHz, a load of 0 N, preload of 60 N), and four groups of different frequencies of 51.7 kHz, 52.2 kHz, 52.7 kHz and 53.2 kHz (500Vp-p, a load of 0 N, preload of 30 N) respectively for the simulation. The relationships between the velocity and various inputs including preload, frequency are shown in Figure 11. Firstly, the proposed motor can realize effective linear motion with a good performance. Secondly, the proposed motor reaches a maximum velocity of 510 mm/s at the frequency of 52.2 kHz and the preload of 30 N. Moreover, the velocity declines with the increase of preload as indicated in Figure 11a. Meanwhile, when the velocity reaches its maximum at the frequency of 52.2 kHz, it begins to decline and rapidly declines to 99 mm/s at the frequency of 53.2 kHz. Besides, it can be obtained from the curve that the proposed motor generally takes about 1.5 milliseconds from power on to the steady state, indicating that it responds quickly.

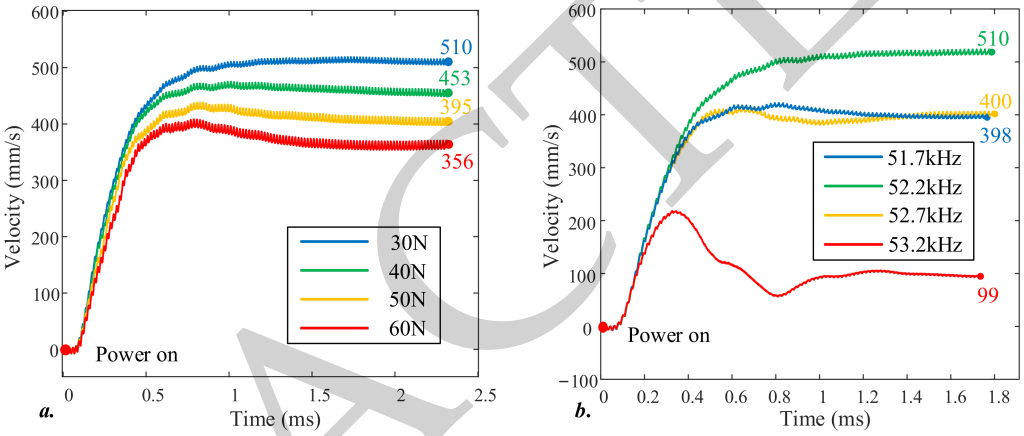


Figure 11. The velocity-time curve of the traveling wave LUSM by simulations: (**a**) the velocity-time curves with different preloads; (**b**) the velocity-time curves with different frequencies.

A prototype of the proposed traveling wave LUSM and an experimental tested system have been fabricated and established, as shown in Figure 12. Two alternation signals with a phase difference of $\pi/2$ are generated by a signal generator (AFG 3022B; Tektronix Inc., Beaverton, OR, USA), and then they are transformed to four signals with phase differences of 0, $\pi/2$, π, and $3\pi/2$ through the signal reversal module. Next, the voltages are amplified by four power amplifiers (HFVA 153; Technology Co., Ltd., Nanjing, China) respectively. When the motor works, its velocity is measured by optical linear encoders, while the load is supplied by several weights.

The load performance of the traveling wave LUSM is simulated (500Vp-p, 52.2 kHz, and preload of 30 N) and the results are shown in Figure 13a. It can be seen that the maximum load can reach 8 N. However, the simulation results are better than the experimental results measured under the same conditions as shown in Figure 13b. Several reasons may account for this phenomenon: the errors in the fabrication and assembly of the prototype occur, which reduces its performance; the simplified finite element model ignores the setting of some contact surfaces such as the contact of the fixing part with the base and ignores the influence of bonding layer on stator's vibration; the setting of simulation parameters such as damping ratio and Coulomb friction coefficient may be inconsistent with the reality. Next, we will focus on improving the accuracy of the finite element model and the performance of the proposed traveling wave LUSM. Even so, this finite element model is of great significance to the performance prediction and working principle verification of the novel motor. Moreover, this model also provides a powerful tool for analyzing the complex non-linear contact mechanism of LUSMs. Thus, in Section 3.3, the contact characteristics between the stator and the slider are discussed from different perspectives in detail to comprehend the operating mechanism of the motor.

RETRACTED

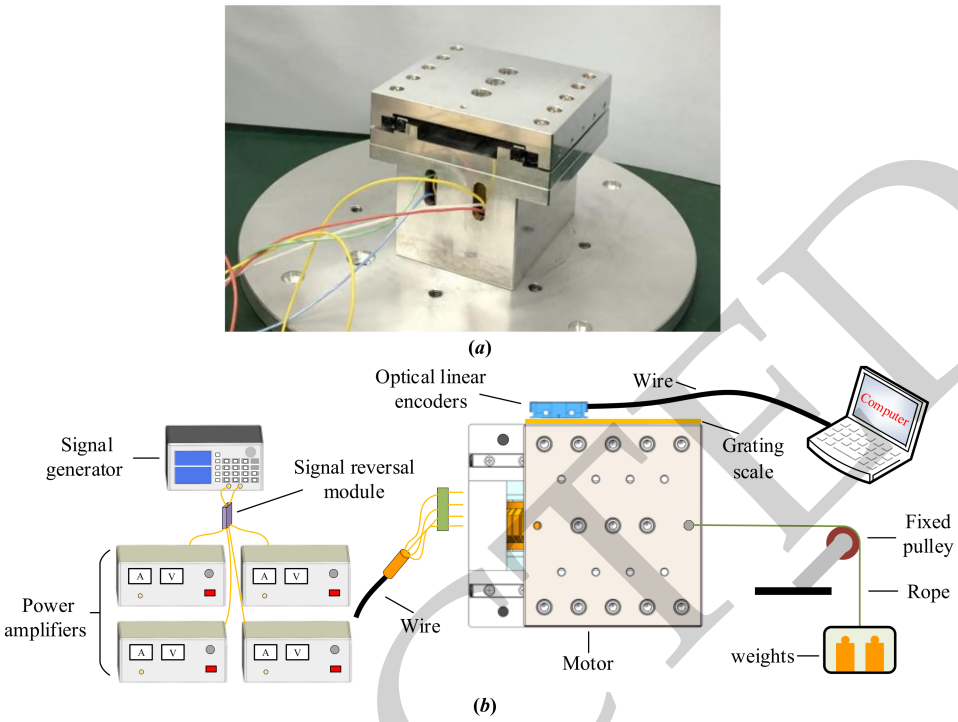


Figure 12. The experimental platform: (**a**) a prototype of the proposed LUSM; (**b**) an experimental tested system.

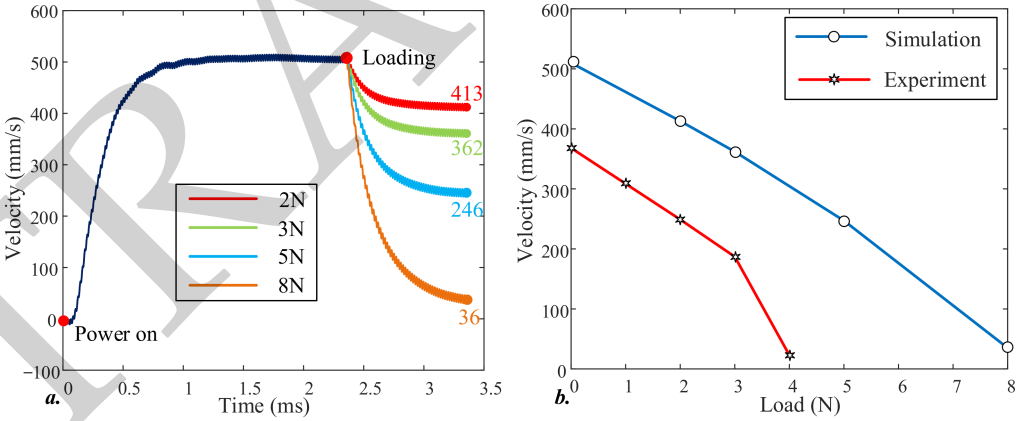


Figure 13. The velocity-load curve of the LUSM by simulations: (**a**) the velocity-time curves with different loads; (**b**) comparison between simulation results and experimental data.

3.3. Contact Characteristic Analysis

In order to better comprehend the operating mechanism of the motor, we need to know the contact characteristics between the stator and the slider. First of all, the process of the traveling wave LUSM from power on to a steady state to power-off ($500V_{p\text{-}p}$, 52.2 kHz, a load of 0 N, preload of 60 N) has been simulated to analyze the contact characteristic. What shows in Figure 14 are the time-domain responses of the velocity, the displacement, and the contact force (normal force and tangential force) between the stator and the slider. Figure 14b indicates that the envelope amplitude of the contact force in the transient state has low-frequency oscillations until the steady state. It is worth noting that when the motor is powered off, the amplitude of the contact force will not decrease linearly, but nonlinear low-frequency oscillation will occur until it reaches 0. Meanwhile, a low-frequency oscillation of the speed of the motor around 0 exists. After about 1.5 ms, the motor stops completely.

RETRACTED

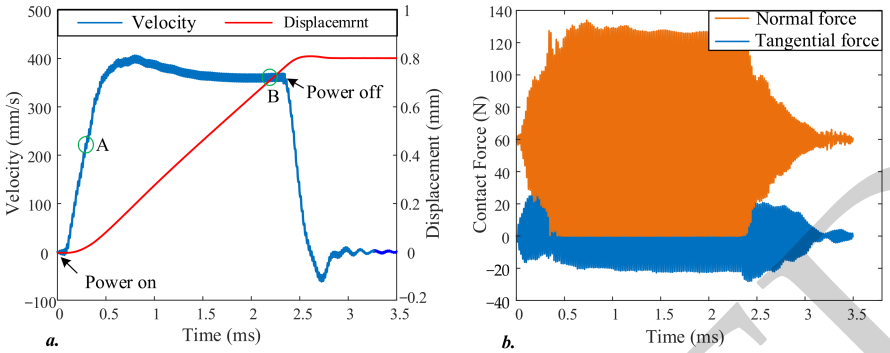


Figure 14. The On/off transients response of the LUSM by simulation: (**a**) the time-domain responses of the velocity and displacement; (**b**) the time-domain responses of the contact force.

Two time periods in the transient state and the steady state, A and B marked in Figure 14a, have been selected to study the contact characteristic in detail. Figure 15 shows the time-domain response of the contact force (normal force and tangential force) and the velocity of the slider in period A and period B, respectively. In order to analyze the contact characteristics between the stator and the slider in a driving cycle T (that is, the stator driving surface performs a complete elliptical motion), we divided a cycle into several stages. In Figure 15a, t_1 to t_4 is a cycle T, and in Figure 15b, t_1 to t_5 is a cycle T. It can be seen from Figure 15a that the amplitude of the normal contact force has been positive for a period, indicating that the stator is not separated from the slider when performing the elliptical motion. What is different from that shown in Figure 15b is the amplitude of the normal contact force is zero during the period of t_4-t_5, which indicates that the stator is separated from the slider.

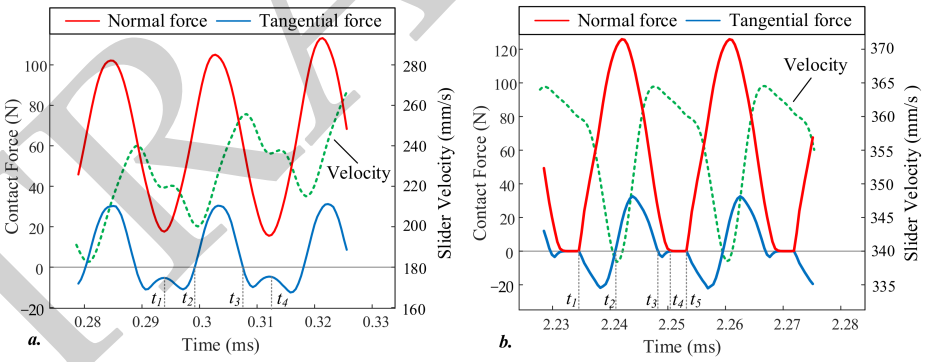


Figure 15. The time-domain response of the contact force and slider velocity: (**a**) period A in the transient state; (**b**) period B in the steady state.

In Figure 15a, the tangential contact force on the slider is negative during t_1-t_2 and t_3-t_4, while it is positive during t_2-t_3, indicating that the driving effect of the stator driving surface on the slider is obstruction-drive-obstruction. The same situation also appears in Figure 15b, the driving effect of the stator driving surface on the slider is obstruction-drive-obstruction- separation. As shown by the slider velocity in Figure 15, when the amplitude of the tangential contact force is negative and zero, the velocity decreases, and when it is positive, the velocity increases. However, from one cycle T in Figure 15a, the positive work done by the tangential contact force of the slider is much more than the negative work, which can explain the reason why the velocity of the slider increases rapidly during the startup phase.

Figure 16 shows the elliptical motion trajectory of point 2 (Figure 10) in the XY plane during the periods of A and B, and the time marks on the trajectory are consistent with Figure 15. On the one hand, it can be found that the size and direction of the elliptical trajectory in Figure 16b and the elliptical trajectory in Figure 10b have changed significantly

RETRACTED

due to the effect of contact. On the other hand, from the results in Figure 16, it can be seen that the elliptical trajectory of the XY plane has a significant change in direction, but the size does not change much. The variation of direction states the phase difference of displacement response in X and Y directions is changed by the contact effect [22].

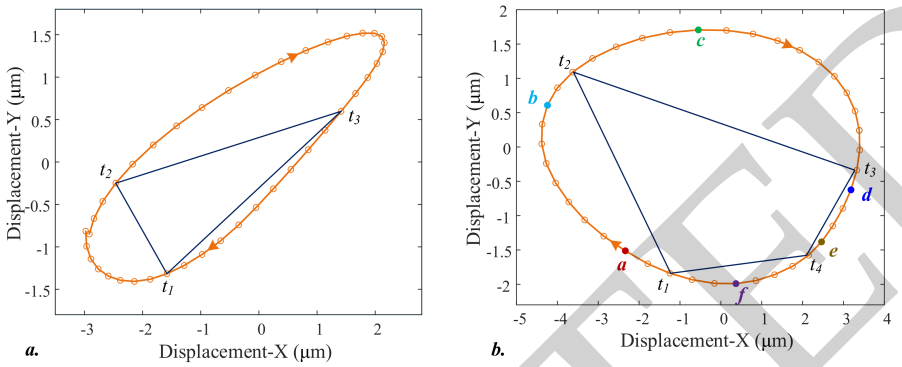


Figure 16. The elliptical motion trajectory: (**a**) period A in the transient state; (**b**) period B in the steady state.

The friction material bonded on the driving tooth was selected as the research object. The diagram of magnified deformation of the friction material at six different positions on the elliptical trajectory and the state of sticking-slipping-separation on the contact surface between the friction material and the slider are demonstrated in Figure 17. At position a, the friction material has just contacted the slider, and the contact surface is in a slip state. Then, the friction material sticks to the slider and the elastic deformation occurs as shown in Figure 17b. Significantly, the contact surface changes from sticking to slipping at time t_2. At position c, the static friction force reaches a critical value, the friction material deforms to the maximum stated in Figure 17c, and the whole contact surface is in a slip state. From time t_3 to t_4, as shown in Figure 17d,e, the contact surface is converted from slipping to sticking and then to slipping. In the end, the friction material separates from the slider at time t_4, and it comes into contact with the slider again at time t_1. In one driving cycle, the contact surface undergoes such a process of slipping-sticking-slipping-sticking-slipping-separation.

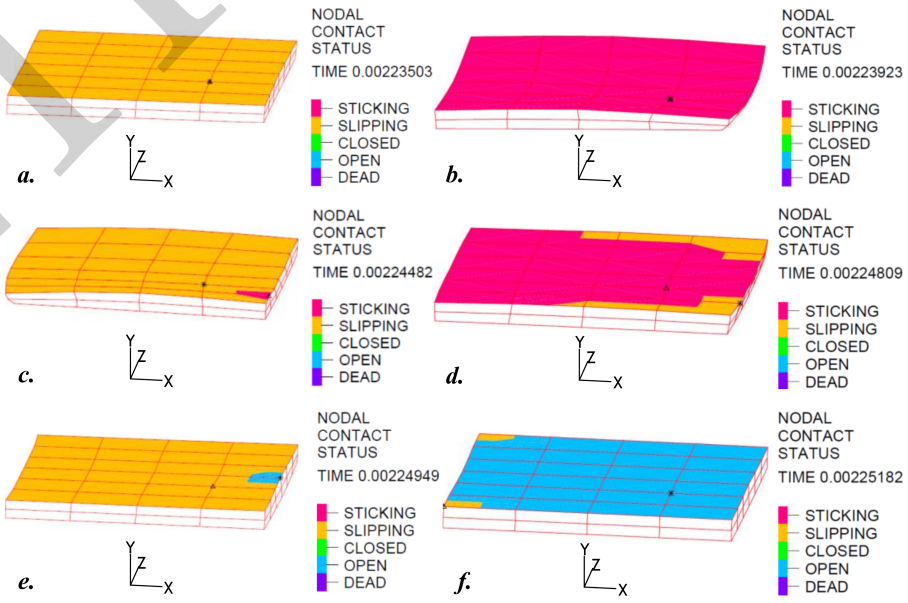


Figure 17. The contact state of the friction material in one driving cycle: (**a**) the slip state; (**b**) the stick state; (**c**) the slip state; (**d**) the stick state; (**e**) the slip state; (**f**) the friction material separates from the slider.

RETRACTED

4. Conclusions

A novel traveling wave linear ultrasonic motor using two orthogonal bending vibration modes is was proposed and simulated by the software ADINA in this paper, and the developed prototype was fabricated and measured with a stator including out-of-plane and in-plane 5th order bending vibration mode. With this finite element model, we verified the novel traveling wave LUSM's operating principle and analyzed the state of sticking-slipping-separation on the contact surface and output performance of the motor in detail. Moreover, the experimental results indicate that the resonance frequencies of Mode-A and Mode-B are 52,062 Hz and 52,093 Hz, respectively, which is almost in accordance with the simulation results. By referring to the ring-type stator of rotary ultrasonic motors, the design of the motor is simplified and the installation of the stator becomes easy. Moreover, there aren't major changes in the frequency differences of Mode-A and Mode-B after installation because of its node circles and node diameters, meaning that the traveling wave we excited is standard so that the precision of the motor can be high with one driving foot.

The motor is in the initial proposal stage and has not yet been optimized thus there are many defects, such as the actual amplitude of the stator being smaller than the simulation result. However, we will improve the structure of the motor based on the simulation results according to the problems found in the experiments in future work.

Author Contributions: Conceptualization, L.Y. and L.C.; Data curation, L.C. and W.R.; Formal analysis, L.C. and M.Y.; Funding acquisition, L.Y.; Investigation, M.Y., R.Z. and S.T.; Methodology, K.Y. and L.C.; Project administration, L.Y. and W.R.; Resources, L.C. and M.Y.; Software, W.R.; Supervision, L.Y.; Validation, L.Y., K.Y. and L.C.; Visualization, K.Y.; Writing—original draft, K.Y. and L.C.; Writing—review & editing, K.Y. and W.R. All authors have read and agreed to the published version of the manuscript.

Funding: This work was supported by the Foundation of Graduate Innovation Center in NUAA (grant No.kfjj20190105), the Priority Academic Program Development of Jiangsu Higher Education Institutions (PAPD), the National Natural Science Foundation of China (Grant Nos. 51905262, and U2037603), and the Natural Science Foundation of Jiangsu Province (Grant No. BK20190398).

Institutional Review Board Statement: Not applicable.

Informed Consent Statement: Not applicable.

Data Availability Statement: Not applicable.

Conflicts of Interest: The authors declared no potential conflicts of interest with respect to the research, authorship, and/or publication of this article.

References

1. Zhao, C. *Ultrasonic Motors: Technologies and Applications*; Springer Science & Business Media: Berlin/Heidelberg, Germany, 2011.
2. Mo, J.S.; Qiu, Z.C.; Wei, J.Y.; Zhang, X.M. Adaptive positioning control of an ultrasonic linear motor system. *Robot. Comput. Integr. Manuf. Int. J. Manuf. Prod. Process Dev.* **2017**, *44*, 156–173. [CrossRef]
3. Yu, P.; Wang, L.; Jin, J.; Ye, Z.; Chen, D. A novel piezoelectric actuated underwater robotic finger. *Smart Mater. Struct.* **2019**, *28*, 105047. [CrossRef]
4. Wai, R.J.; Lee, J.D. Comparison of Voltage-Source Resonant Driving Schemes for a Linear Piezoelectric Ceramic Motor. *IEEE Trans. Ind. Electron.* **2008**, *55*, 871–879. [CrossRef]
5. Ryndzionek, R.; Sienkiewicz, L. A review of recent advances in the single- and multi-degree-of-freedom ultrasonic piezoelectric motors. *Ultrasonics* **2021**, *116*, 106471. [CrossRef] [PubMed]
6. Uchino, K. The Development of Piezoelectric Materials and the New Perspective. In *Advanced Piezoelectric Materials*; Woodhead Publishing: Cambridge, UK, 2017; pp. 1–92.
7. Koc, B.; Von Deyn, L.; Delibas, B. Dual Source Dual Frequency Drive and Modeling of Resonance type Piezoelectric Motors. In Proceedings of the ACTUATOR, International Conference and Exhibition on New Actuator Systems and Applications, Mannheim, Germany, 17–19 February 2021; pp. 1–4.
8. Li, X.; Yao, Z.; Li, R.; Wu, D. Dynamics modeling and control of a V-shaped ultrasonic motor with two Langevin-type transducers. *Smart Mater. Struct.* **2019**, *29*, 25018. [CrossRef]
9. Li, X.; Yao, Z.; Yang, M. A novel large thrust-weight ratio V-shaped linear ultrasonic motor with a flexible joint. *Rev. Sci. Instrum.* **2017**, *88*, 65003. [CrossRef] [PubMed]

RETRACTED

10. Li, X.; Yao, Z.; Wu, R. Modeling and analysis of stick-slip motion in a linear piezoelectric ultrasonic motor considering ultrasonic oscillation effect. *Int. J. Mech. Sci.* **2016**, *107*, 215–224. [CrossRef]
11. Li, H.; Tian, X.; Shen, Z.; Li, K.; Liu, Y. A low-speed linear stage based on vibration trajectory control of a bending hybrid piezoelectric ultrasonic motor. *Mech. Syst. Signal Processing* **2019**, *132*, 523–534. [CrossRef]
12. Zhang, Q.; Chen, H.J.; Liu, Y.X.; Wang, W.Z.; Zhang, H.; Zhou, X.Y.; Chen, D.L.; Wang, M.N. A bending hybrid linear piezoelectric actuator using sectional excitation. *Sens. Actuators A-Phys.* **2018**, *271*, 96–103. [CrossRef]
13. Liu, Y.; Chen, W.; Liu, J.; Yang, X. A High-Power Linear Ultrasonic Motor Using Bending Vibration Transducer. *IEEE Trans. Ind. Electron.* **2013**, *60*, 5160–5166. [CrossRef]
14. Jipeng, Y.; Yingxiang, L.; Junkao, L.; Dongmei, X.; Weishan, C. The design and experiment of a novel ultrasonic motor based on the combination of bending modes. *Ultrasonics* **2016**, *71*, 205–210.
15. Yin, Z.; Dai, C.; Cao, Z.; Li, W.; Li, C. Modal analysis and moving performance of a single-mode linear ultrasonic motor. *Ultrasonics* **2020**, *108*, 106216. [CrossRef] [PubMed]
16. Lu, D.; Lin, Q.; Chen, B.; Jiang, C.; Hu, X. A Single-modal Linear Ultrasonic Motor based on Multi Vibration Modes of PZT Ceramics. *Ultrasonics* **2020**, *107*, 106158. [CrossRef] [PubMed]
17. Liu, Z.; Yao, Z.; Jian, Y.; Li, X. A novel plate type linear piezoelectric actuator using dual-frequency drive. *Smart Mater. Struct.* **2017**, *26*, 95016. [CrossRef]
18. Ren, W.; Yang, L.; Ma, C.; Li, X.; Zhang, J. Output performance simulation and contact analysis of traveling wave rotary ultrasonic motor based on ADINA. *Comput. Struct.* **2019**, *216*, 15–25. [CrossRef]
19. Ma, X.; Liu, J.; Deng, J.; Liu, Q.; Liu, Y. A Rotary Traveling Wave Ultrasonic Motor With Four Groups of Nested PZT Ceramics: Design and Performance Evaluation. *IEEE Trans. Ultrason. Ferroelectr. Freq. Control* **2020**, *67*, 1462–1469. [CrossRef] [PubMed]
20. Jingzhuo, S.; Bo, L. Optimum Efficiency Control of Traveling-Wave Ultrasonic Motor System. *IEEE Trans. Ind. Electron.* **2011**, *58*, 4822–4829.
21. Yang, L.; Ren, W.; Ma, C.; Chen, L. Mechanical simulation and contact analysis of the hybrid longitudinal-torsional ultrasonic motor. *Ultrasonics* **2020**, *100*, 105982. [CrossRef] [PubMed]
22. Zhang, J.; Yang, L.; Chen, H.; Ma, C.; Chen, L. Design of Travelling-Wave Rotating Ultrasonic Motor under High Overload Environments: Impact Dynamics Simulation and Experimental Validation. *Appl. Sci.* **2019**, *9*, 5309. [CrossRef]

RETRACTED